Journal of Materials Chemistry A

ROYAL SOCIETY OF CHEMISTRY

PAPER

View Article Online
View Journal | View Issue

Check for updates

Cite this: J. Mater. Chem. A, 2021, 9, 16889

An efficiency of 14.29% and 13.08% for 1 cm^2 and 4 cm^2 flexible organic solar cells enabled by sol–gel ZnO and ZnO nanoparticle bilayer electron transporting layers†

Wei Pan,‡[ab] Yunfei Han,‡[a] Zhenguo Wang,[a] Chao Gong,[a] Jingbo Guo,[a] Jian Lin,[a] Qun Luo, *[a] Shangfeng Yang [bc] and Chang-Qi Ma [a]

Received 20th April 2021
Accepted 2nd July 2021

DOI: 10.1039/d1ta03308e

rsc.li/materials-a

Flexible organic solar cells (OSCs) will be a promising energy harvest approach for portable and wearable electronics. However, the efficiency of flexible OSCs, particularly the efficiency of flexible devices with an area larger than 1 cm^2, is still limited due to the lack of good flexible electrodes and the inhomogeneity of the large-area films. In this work, higher sensitivity of the performance to the interface contact for large-area devices (1 and 4 cm^2) than small area devices (0.09 cm^2) was found in flexible OSCs with different areas. To address this issue, a bilayer electron transporting layer (ETL) combining a lower sol–gel ZnO and an upper ZnO nanoparticle layer was developed for silver nanowire (AgNW) electrode involving large-area flexible OSCs. The use of the lower sol–gel ZnO layer effectively filled the network voids and modified the surface energy of the AgNWs, which enabled the homogeneous coverage of the upper ZnO nanoparticle layer and enhanced carrier collection. Due to the more homogeneous films and improved interface charge collection, the use of the sol–gel ZnO and ZnO NP bilayer ETL has lowered the performance decrease during upscaling. A record efficiency of 14.29% and 13.08% for the 1 and 4 cm^2 flexible OSCs was achieved.

Introduction

Organic solar cells (OSCs) are attracting much attention due to their advantages of light weight and flexibility.[1] In recent years, with the rapid development of non-fullerene acceptor materials,[2–4] the performance of OSCs has improved rapidly. Currently, a single junction solar cell fabricated in the laboratory can typically achieve an efficiency higher than 16%. The highest reported performance has reached over 18%,[5,6] and the certified maximum efficiency is 17.6%.[5] This trend strongly reflects the huge commercialization potential of OSCs. Although the photovoltaic performance of OSCs was continuously improved, the stability and the efficiency of large area cells are still two challenges that limited their practical application.[7]

Regarding flexible OSCs, a flexible electrode with high conductivity and high light transmittance is one of the bases. Flexible ITO,[8,9] metal grids,[10,11] silver nanowires (AgNWs),[12,13] *etc.* are commonly used as the flexible transparent electrodes for flexible OSCs.[14] By comparing the transmittance, bending resistance, and sheet resistance of these various flexible electrodes, it was found the AgNW electrode has good comprehensive properties. In addition, the flexible AgNW electrode has the advantages of low cost, large area, and roll-to-roll printing compatibility. Previously, we have developed gravure printing technology to produce Ag electrodes.[15] Li *et al.* developed a method to create an AgNW network using water-processed silver nanowires and a polyelectrolyte. Due to ionic electrostatic charge repulsion, the nanowires formed grid-like structures, leading to smooth flexible electrodes and improved conduction.[16] In addition, the welding strategy could improve the conduction.[17] With AgNW flexible electrodes, flexible small-area OSCs reached an efficiency of 16.1%[18] and 16.5%[16] for single-junction and tandem devices.

Though AgNW-based flexible OSCs have reached an excellent performance for small sizes, the performance of large-area devices still lags behind that of small-area solar cells.[19–22]

[a]Printable Electronics Research Center, Suzhou Institute of Nano-Tech and Nano-Bionics, Chinese Academy of Sciences (CAS), Suzhou, 215123, P. R. China. E-mail: qluo2011@sinano.ac.cn

[b]Nano Science and Technology Institute, University of Science and Technology of China, 166 Ren Ai Road, SEID SIP, Suzhou, Jiangsu 215123, P. R. China

[c]Department of Materials Science and Engineering, Synergetic Innovation Center of Quantum Information & Quantum Physics, University of Science and Technology of China, Hefei, 230026, P. R. China

† Electronic supplementary information (ESI) available: The topography and phase diagram from AFM and the fitting parameters of electrochemical impedance spectroscopy (EIS). See DOI: 10.1039/d1ta03308e

‡ These authors contributed equally to this work.

Until now, the champion performance of 1 cm^2 flexible OSCs was 13.61%, with gravure-printed AgNWs as the electrode.[15] In contrast, the performance of 0.04 cm^2 small-area OSCs with the same device structure was 15.28%.[15] We know that large-area OSC modules were always connected in series and shunt using single tripe cells with a width of 1–2 cm.[23–27] Thus, the performance of 1 and 4 cm^2 cells is quite important, which would decide the module performance.[22] Through investigating and optimizing the performance of 1 or 4 cm^2 cells, we can find the critical influencing factors of large-area OSCs, and deeply understand the basic scientific issue for improving the performance of large-area solar cells. Based on the optimization of 1 and 4 cm^2 cells, a higher efficiency of large-area module devices could be expected. Regarding the lower efficiency of 1 or 4 cm^2 flexible devices, it is mainly due to the large resistance of the transparent electrodes.[28–30] Meanwhile, the uniformity of the films[31,32] and the large contact resistance of different functional layers are two influencing factors as well.[33] The surface of AgNW network electrodes is much rougher than that of the conventional ITO electrode due to the intricate stacking of silver wires on the substrate, which may lead to poor reproducibility and uniformity. Generally, highly conductive PEDOT:PSS is introduced as a sacrificial layer on the top of the AgNWs to fill the gap of the silver wire and make the electrode surface smooth.[34] Using such a modification, reasonable performance has been reported in previous work.[35] However, in inverted OSCs, as AgNWs were used as the cathode, ZnO with a working function of around 4–4.4 eV is used as the electron transporting layer (ETL) of the cathode. When PEDOT:PSS is inserted as a sacrificial layer between the cathode and ZnO ETL, charge transfer and collection will be affected, and quick oxidation of Ag electrode existed, which would cause low performance and inferior device stability.[36]

Considering the poor interface contact between AgNWs and ZnO, we developed a bilayer ETL based on sol–gel ZnO and ZnO nanoparticles as an improvement. Previously, several studies have reported that the use of a bilayer ETL based on ZnO and polymer or small molecules could suppress the interfacial energy barrier,[37] form interfacial dipoles,[38] regulate the surface work function,[39] lead to the formation of well-defined nano–micro phase separation morphology of the active layer,[39] *etc.* In this work, sol–gel ZnO films were used to cover the surface of AgNW electrodes[40] as an alternative instead of PEDOT:PSS, to solve the problem of unmatching of the energy level and poor interface contact between PEDOT:PSS and ZnO. Meanwhile, we focused on 1 and 4 cm^2 cells in order to solve the critical issue for high-performance large-area single cells. Through comparing flexible OSCs of different sizes, a higher sensitivity of 1 and 4 cm^2 devices than the small-area device was observed. The use of the lower sol–gel ZnO layer effectively filled the network voids and modified the surface energy of the AgNWs, which enabled the homogeneous coverage of the upper ZnO nanoparticle layer and enhanced charge carrier collection. Thus, the solar cells based on the bilayer ETL can achieve excellent photoelectric performance. More importantly, a decrease of performance during upscaling was observed. A record performance of 14.29% and 13.08% for the 1 and 4 cm^2 cells was achieved with such a bilayer ETL.

Results and discussion

First of all, we investigated the influence of different ETLs on the electrode properties by testing the transmittance spectra and sheet resistance of the flexible electrodes. PET/AgNWs, PET/AgNWs/sol–gel ZnO, PET/AgNWs/ZnO NP, and PET/AgNWs/sol–gel ZnO/ZnO NP films were fabricated. PET/AgNWs electrodes were prepared by gravure printing.[15] The thickness and the density of the AgNWs were regulated through changing the printing times, and printing time related sheet resistance and T_{550} (transmittance at 550 nm) are showed in Fig. 1(a). For optimization, AgNWs with a sheet resistance of about 10 Ω sq^{-1} and a T_{550} of 80% (including the substrate) from two times printing were selected. Sol–gel ZnO films were prepared through spin coating a precursor solution containing ethanolamine, 2-methoxyethanol, and alcohol acetate dihydrate on the top of the AgNWs. ZnO NPs were deposited on the top of the sol–gel ZnO films through spin coating a 15 mg mL^{-1} ZnO NP solution. The transmission spectra are shown in Fig. 1(b). The average transmittance of the PET/AgNW film in the 550–1000 nm wavelength range is about 80%. The transmittance in the range of 380–1000 nm remained almost unchanged after modification with sol–gel ZnO, which is because of the high light transmission of sol–gel ZnO. In addition, the T_{550} of the AgNWs/sol–gel ZnO film was slightly changed with the increase of sol–gel ZnO concentration (Fig. S1†). For the PET/AgNWs/ZnO NP films, the transmittance in the region of 350–1100 nm was significantly reduced. However, in the case of the PET/AgNWs/sol–gel ZnO/ZnO NP film, though the transmittance from 350–400 nm also decreased, the transmittance in the region from 550 to 1100 nm was slightly higher than that of the PET/AgNW films. The UV-vis absorption spectra of the ZnO NPs and sol–gel ZnO films had been tested (Fig. S2†). We found that the absorption intensity of the ZnO NP film was significantly higher than that of sol–gel ZnO films, which led to a low transmittance of PET/AgNWs/ZnO NPs.

The sheet resistances of these different films are shown in Fig. 1(c). The sheet resistance of PET/AgNWs was about 10 Ω sq^{-1}. When the AgNWs were covered by sol–gel ZnO, a slight decrease in the sheet resistance was found, which was because the thin sol–gel ZnO layer could not completely cover the AgNWs. In contrast, sol–gel ZnO would mostly fill in the interspace of the nanowire networks, which is beneficial to smooth the surfaces (proved by the AFM and SEM images, *vide infra*) and improve the connection of AgNWs. So, it was reasonable to observe the slight improvement of conduction. Such a result was observed in both the AgNWs/sol–gel ZnO films with low sol–gel ZnO concentration (0.05 and 0.1 M, shown in Fig. S3†). As the concentration of sol–gel ZnO further increased to 0.2 M, the sheet resistance slightly increased, which was because the excess ZnO covered the top of AgNWs. The SEM images (*vide infra*) of AgNWs/ZnO NPs showed the ZnO NPs completely covered the top of AgNW networks rather than enter into the interspace of AgNWs. Thus, increases of the sheet resistance to around 20–25 Ω sq^{-1} for the AgNWs/

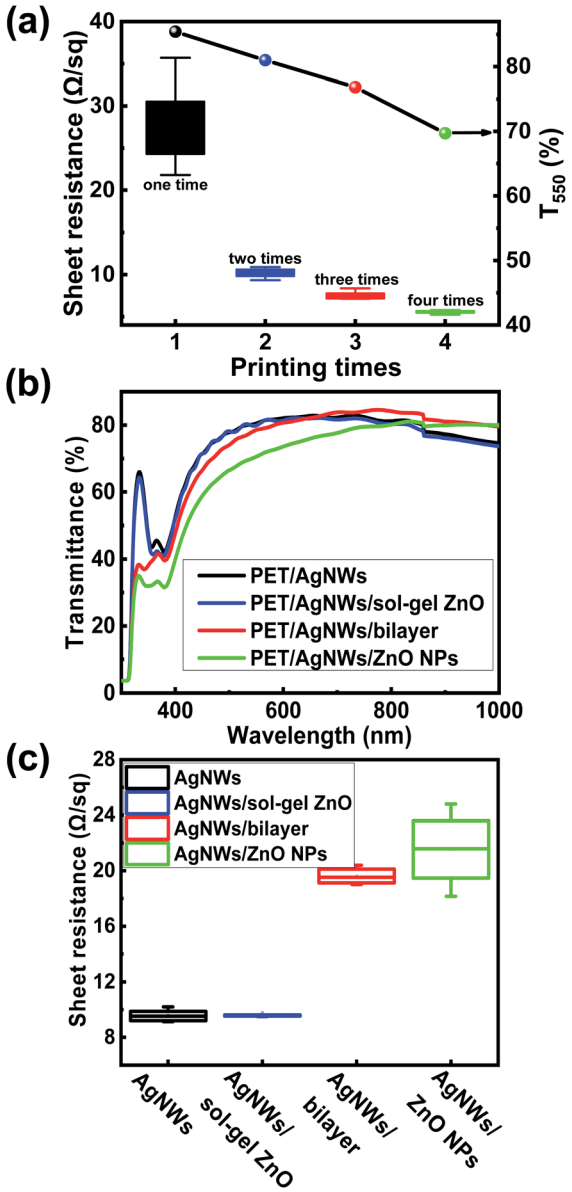

Fig. 1 (a) The sheet resistance and T_{550} of PET/AgNW electrodes fabricated by gravure printing for different times, (b) UV-vis absorption spectra and (c) the sheet resistance of the PET/AgNW, PET/AgNWs/sol–gel ZnO, PET/AgNWs/ZnO NP, and PET/AgNWs/sol–gel ZnO/ZnO NP films.

ZnO and AgNWs/sol–gel ZnO/ZnO NP films were observed. However, the cover of the bilayer film led to a lower sheet resistance compared to the film with only ZnO NPs. These results might imply that the sole ZnO NPs could not effectively enter the interspace of the nanowires due to unfavorable surface energy or the incompatibility between ZnO NPs and the surfactant of AgNW PVP (*vide infra*). Therefore, the thick ZnO NP layer piled on the top of AgNWs and resulted in a more obvious decrease of conduction. For the AgNWs/bilayer films, the precoated sol–gel ZnO layer has regulated the surface energy. In addition, the interspace of the AgNWs has been already filled. Because of these two reasons, the ZnO NPs could be much easier to fill into the residual AgNW interspaces and form more uniform films. As a consequence, the conduction of AgNWs/bilayer was better than that of the AgNWs/ZnO NPs.

To study the reason of conduction variation with different ETLs, the contact angle between the ZnO solution and the PET/AgNW electrode was firstly tested. As shown in Fig. 2(a) and (b), the contact angle between sol–gel ZnO solution and the pristine AgNW electrode was about 23.7°, and the contact angle of ZnO NP solution on the top of the AgNWs was about 36.5°. This result showed that sol–gel ZnO had a better compatibility with AgNWs than ZnO NPs, which would enable better film quality of the AgNWs/sol–gel ZnO films. In addition, the contact angle of ZnO NPs on the top of AgNWs/sol–gel ZnO was also tested (Fig. 2(c)). It was obvious that the modification of the AgNW electrode with sol–gel ZnO increased the wettability between the electrode and ZnO NP solution, making ZnO NPs easier to be spread on the top of the electrode during the spin coating process. The surface morphology of AgNWs, AgNWs/sol–gel ZnO, AgNWs/ZnO NPs, and AgNWs/sol–gel ZnO/ZnO NPs was also investigated by using the scanning electron microscope (SEM) images and is shown in Fig. 2(d) and (g). For the AgNWs/ZnO NP films, a circular area (in the 35-magnification image, as shown in Fig. 2(f)) can be observed, which was the aggregation of ZnO NPs due to the poor wettability of ZnO NP solution on the AgNW electrode. In these ripple regions, the ZnO NPs might be thicker and rougher. Meanwhile in the thin region, some obvious cavities were observed in the ZnO films (as shown in the 20 K and 50 K magnification images). The ZnO NPs on the top of AgNWs/sol–gel ZnO films were much homogeneous as shown by the SEM images (Fig. 2(g)). Nearly no cavities and large particles were found. The improved homogeneity of ZnO NPs on the top of AgNWs/sol–gel ZnO could be ascribed to the better compatibility between ZnO NPs and sol–gel ZnO, which enhances the spreading of ZnO NPs during spin-coating.

Furthermore, the atomic force microscopy (AFM) images of the AgNW, AgNWs/sol–gel ZnO, AgNWs/sol–gel ZnO/ZnO NP, and AgNWs/ZnO NP films were studied. The topography and phase diagram from AFM are shown in Fig. S4.† There were enormous gaps between Ag nanowire networks in the bare AgNW electrode and the root-mean roughness (RMS) of the AgNW electrode was 8.9 nm. The introduction of a sol–gel ZnO modification layer on the top of AgNWs leads to a decreased RMS of 6.36 nm. The RMS of the AgNWs/sol–gel ZnO/ZnO NP and AgNWs/ZnO NP film was 7.5 and 7.7 nm, respectively. From these results, we found that the depositing of sol–gel ZnO leads to the decrease of RMS because the gap of the AgNW network was filled by the sol–gel ZnO, which could be proved by the phase images of AgNW and AgNWs/sol–gel ZnO films. Despite the imperfect coverage of ZnO on AgNWs, sol–gel ZnO penetrated the interspace of the AgNW network and improved the charge collection in the horizontal direction. The covering of AgNWs both by ZnO NPs and sol–gel ZnO/ZnO NPs showed a similar surface roughness. However, the phase diagram showed that the films modified with sol–gel ZnO/ZnO NPs are more uniform than the sole ZnO NP-based films though the two films have nearly the same roughness. Thus, the improved uniformity might be the underlying reason for performance and

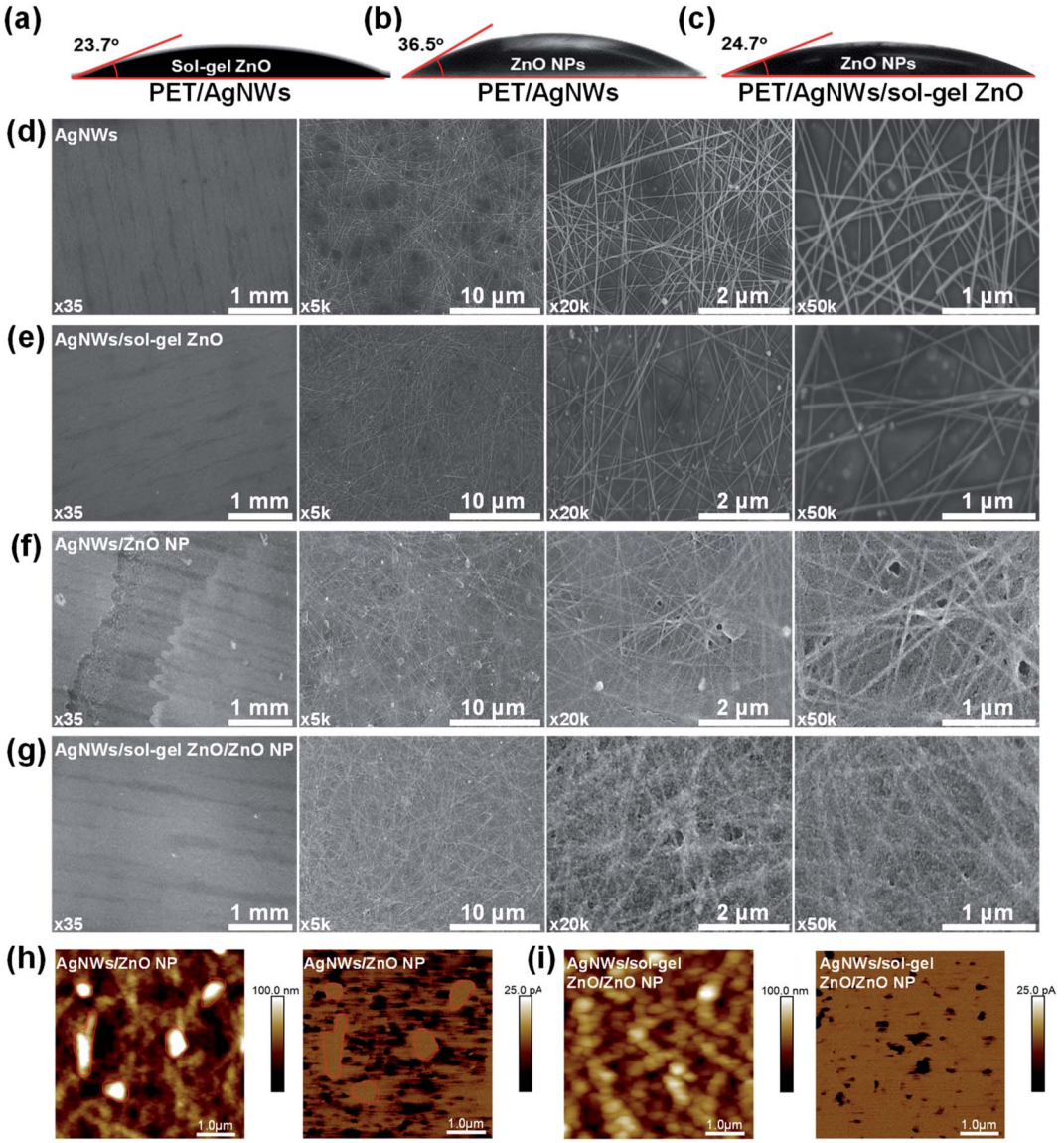

Fig. 2 Photographs of a drop of sol–gel ZnO inks on the top of (a) the AgNWs, photographs of a drop of ZnO NP nanoinks on the top of (b) the AgNWs, and (c) AgNWs/sol–gel ZnO films, SEM images of (d) the AgNW, (e) AgNWs/sol–gel ZnO, (f) AgNWs/ZnO NP, and (g) AgNWs/sol–gel ZnO/ZnO NP films, and CAFM images of (h) AgNWs/sol–gel ZnO and (i) AgNWs/sol–gel ZnO/ZnO NP films.

reproducibility improvement of 1 cm^2 solar cells. Then in order to study the current uniformity of different films, we tested the C-AFM current of the AgNWs/sol–gel ZnO/ZnO NP and AgNWs/ZnO NP films. The topography and current of C-AFM are shown in Fig. 2(h) and (i). The inhomogeneous area (the part of the red circle) of the topography and the current mapping of the AgNWs/ZnO NP film were consistent. Darker contrast indicated less current flowing in the large ZnO NP particle region in the AgNWs/ZnO NP films. Based on the AFM and SEM images of these films, we knew that modifying the AgNWs with sol–gel ZnO with a low concentration caused a slight decrease of the sheet resistance, which was due to the improved interconnection of the AgNWs. The metal oxides could penetrate into the interspace of the AgNW network and improve the charge collection. Similar results had been reported in previous work.[17,41–43] Such a modification also significantly improved the electrical homogeneity as proved by the CAFM result.

With the flexible AgNW electrodes, 1 cm^2-flexible OSCs with a structure of PET/AgNWs/ETL/active layer/MoO_3/Al were fabricated. A PBDB-T-2F(PM6):Y6 heterojunction was used as the non-fullerene photoactive layer. Three kinds of ETLs, *i.e.* ZnO nanoparticle (ZnO NP) ETL, sol–gel ZnO ETL, and sol–gel ZnO/ZnO NP bilayer ETLs, were used, and the device performances were compared. Sol–gel ZnO solutions with three different concentrations, *i.e.* 0.05 M, 0.1 M, and 0.2 M, were used. On the top of sol–gel ZnO films, ZnO NPs, an active layer, MoO_3 and Al were deposited. Fig. 3 shows the device structure, photographs, energy levels, *J–V* characteristics, and EQE spectra of the flexible solar cells. The device efficiency is shown in Table 1. From the energy level of the flexible solar cells,[44] we found

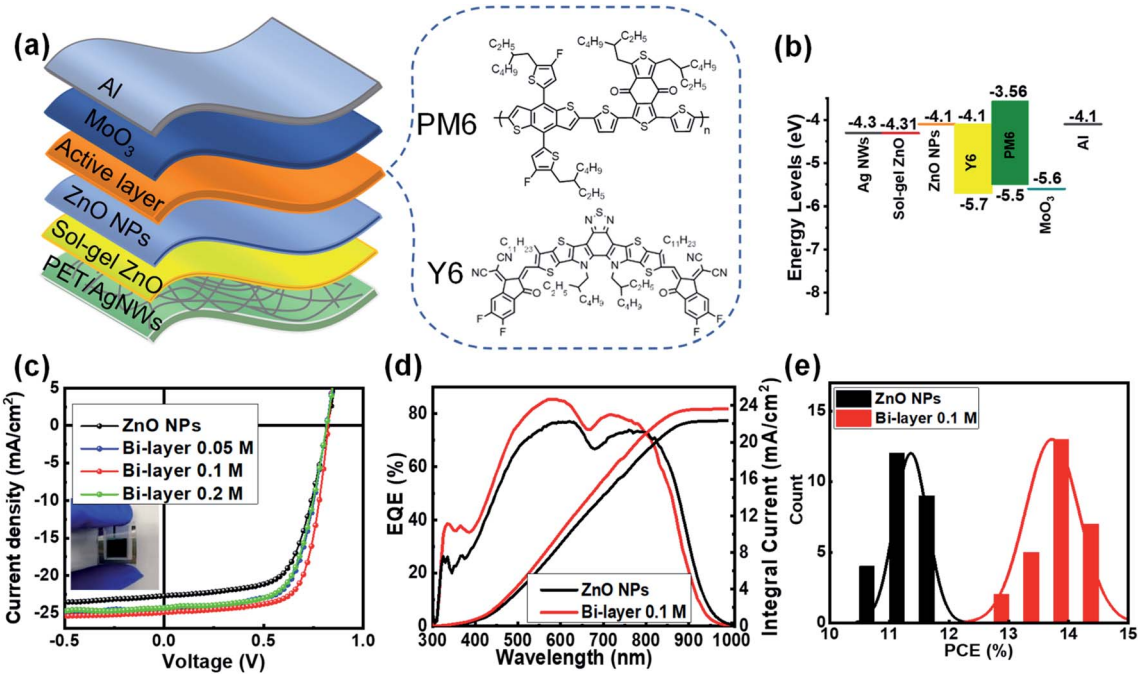

Fig. 3 (a) Device structure, (b) energy levels of the device, (c) photographs and *J*–*V* characteristics, (d) EQE spectra, and (e) the histogram of the 1 cm^2 flexible OSCs.

Table 1 Device performance of the 1 cm^2 flexible solar cell with different ETLs

Area	ETLs	V_{OC} (V)	J_{SC} (mA cm^{-2})	FF	PCE_{max} (%)	PCE_{ave} (%)	R_S (Ω cm^2)	R_{Sh} (Ω cm^2)
1 cm^2	ZnO NPs	0.82	22.70	0.63	11.73	11.61 ± 0.27	9.0	564.3
	Bi-layer 0.05 M	0.82	24.49	0.66	13.25	13.23 ± 0.03	5.2	750.4
	Bi-layer 0.1 M	0.82	24.89	0.70	14.29	14.00 ± 0.28	4.9	648.8
	Bi-layer 0.2 M	0.82	24.31	0.65	12.95	12.90 ± 0.04	5.6	402.9

that the work functions of the three kinds of ETLs were all suitable for inverted PM6:Y6 solar cells.

The current density–voltage (*J*–*V*) curves of the devices are shown in Fig. 3(c), and the optimized device performance parameters are listed in Table 1. We can see that the optimized device with a sole ZnO NP ETL showed an open circuit-voltage (V_{OC}) of 0.82 V, a short-circuit current density (J_{SC}) of 22.70 mA cm^{-2}, a fill factor (FF) of 63%, and a power conversion efficiency (PCE) of 11.73%. The device with a 0.2 M sol–gel ZnO ETL nearly can't work, which was attributed to the unsuitable photoelectric properties of the amorphous ZnO layer that was fabricated through low-temperature annealing at 150 °C. We know that the sol–gel ZnO ETL is widely used in rigid OSCs and presented excellent device performance. But, the sol–gel ZnO ETL should be fabricated by thermal annealing at 200 °C.[45] The PET/AgNWs/sol–gel ZnO/ZnO NP devices showed a similar V_{OC} of 0.82 V to the ZnO NP ETL device. In the sol–gel ZnO/ZnO NP bilayer, ZnO NPs directly contacted with the active layers and served as the carrier collection layer, while the sol–gel ZnO layer was the modification of the AgNW electrode and provided a guarantee for excellent deposition of the ZnO NP layer in these devices. Though the work functions of the sol–gel ZnO and ZnO NPs have a slight difference, the final surface work function of the sol–gel ZnO/ZnO NP bilayer ETL was the same as that of the ZnO NPs since the surface work function was decided by the upper layer. With the modification of sol–gel ZnO, the bilayer ETL devices presented an improved performance. In addition, the performance showed slight dependence on the concentration of sol–gel ZnO. Specifically, with the increase of sol–gel ZnO concentration, the PCEs of the device increased first and then decreased, with 0.1 M as a saturation point. As an optimized performance, a PCE of 14.29% with a V_{OC}, J_{SC}, and FF of 0.82 V, 24.89 mA cm^{-2}, and 70% was observed. The external quantum efficiency (EQE, Fig. 3(d)) spectra of the OSCs showed an integrated current of 24.43 mA cm^{-2} for the optimized device, in good agreement with the value obtained from *J*–*V* curves. In addition, from Table 1, we found that the concentration of the sol–gel ZnO films impacted J_{SC} and FF. According to the series resistance (R_S) and shunt resistance (R_{Sh}) of these devices, we know that the devices based on bilayer ETLs have smaller R_S than the device with a ZnO NP ETL. Additionally, among these devices with bilayer ETLs, the optimized device (with 0.1 M sol–gel ZnO) had the lowest R_S. The decreased R_S might be due to the smaller contact resistance due to the improvement of

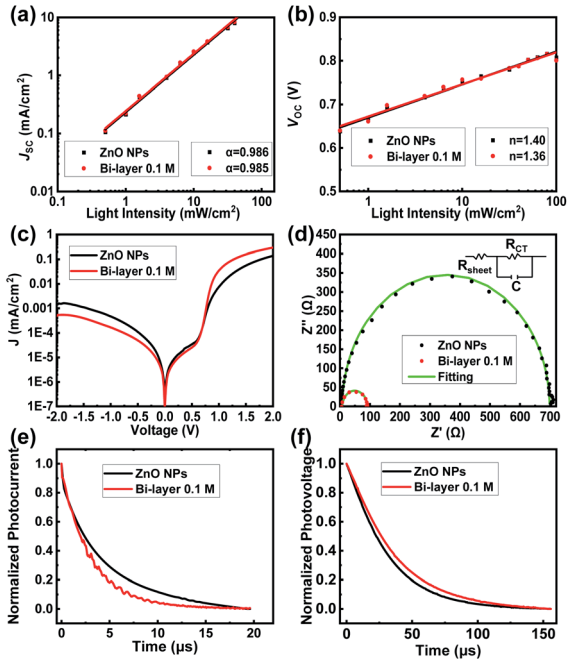

Fig. 4 (a) Light intensity dependent J_{SC}, (b) V_{OC}, (c) dark J–V curves, (d) impedance, (e) normalized TPC, and (f) TPV of the 1 cm^2 flexible OSCs with ZnO NP and sol–gel ZnO/ZnO NP bi-layer ETLs.

interface contact between the Ag nanowires and the buffer layer by the use of the bilayer ETL. From the performance histogram (Fig. 3(e)) of the optimized performance, we observed that the statistical PCE of the ZnO NP ETL-involving device was between 10.86% and 11.73%, while the efficiency of the device based on the sol–gel ZnO/ZnO NP bilayer ETL improved to 12.87–14.29%.

The light intensity dependent V_{OC} and J_{SC} of the two devices were analyzed. Fig. 4(a) shows the light intensity dependent J–V characteristics of the 1 cm^2 solar cells with different ETLs. Among them, J_{SC} is linearly related to light intensity, and the slope α is about 0.985 and 0.986, which indicated that the effect of bimolecular charge recombination and the space charge effect on the device was negligible in these devices. At the same time, V_{OC} also has a linear relationship with light intensity in Fig. 4(b). The ideal factor n could be calculated using the equation of $V_{OC} = (nk_BT/q)\ln(J_{ph}/J_0 + 1)$, where k_B is the Boltzmann constant, T is the temperature and J_0 is the reverse saturation current density.[46] The n value was 1.40 and 1.36 for the ZnO NP and sol–gel ZnO/ZnO NP ETL-based devices. The dark J–V curve and the electrochemical impedance spectroscopy (EIS) spectra of the 1 cm^2 flexible solar cells were further recorded. From Fig. 4(c), we found that the device with a bilayer ETL showed a higher rectification ratio than the device with a sole ZnO NP ETL, suggesting improved charge selectivity of the solar cells with a bilayer ETL. Such a result was in good agreement with the improved FF of the device with a bilayer ETL. In addition, we found that all the semicircles of the EIS spectra could be simulated using the same circuit model (as shown in the analog circuit in the inset of Fig. (d)). In this model, the series resistance was composed of sheet resistance of the electrode (R_{sh}) and charge transfer resistance between the electrode and the active layer (R_{CT}) and C is a capacitor. The calculated results of the resistor and capacitor are shown in Table S1.† Chen *et al.*[47] also reported the same impedance circuit model. The results showed that the bi-layer ETL-based device has a lower charge transfer resistance (R_{CT}) of 84.2 Ω than the sole ZnO NP ETL-based device (690.0 Ω), thereby improving the interface charge transport capability, making the devices have a lower series resistance. The transient photocurrent (TPC) and transient photovoltage (TPV) of the devices are shown in Fig. 4(e) and (f) to analyze the charge extraction and recombination process. The charge extraction time of the ZnO and bilayer ETL-based devices was calculated to be 6.02 and 3.15 μs. The shorter charge extraction time of the bilayer ETL

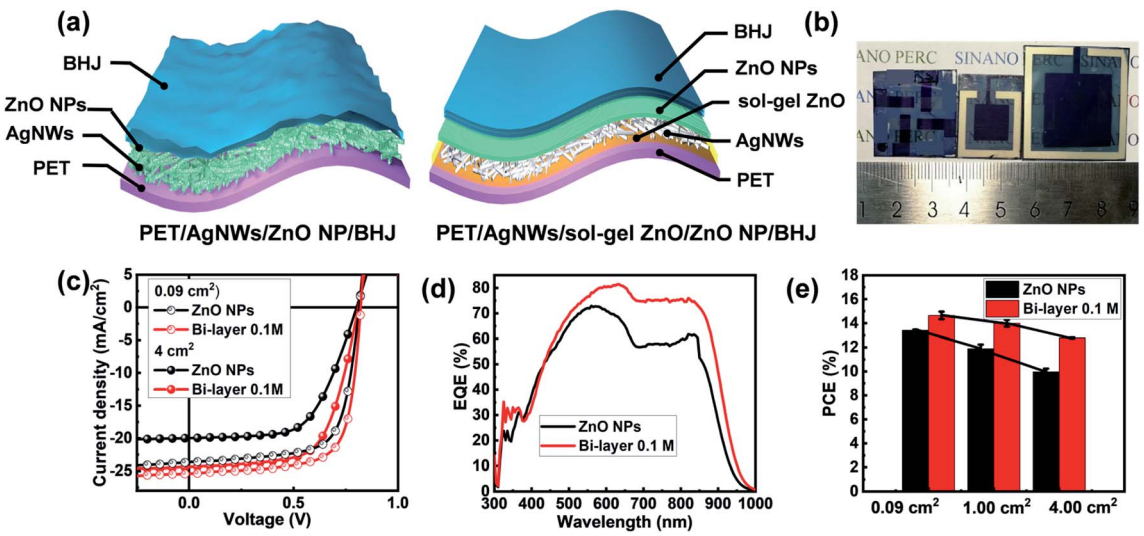

Fig. 5 (a) Schematic diagram of sol–gel ZnO modified AgNWs, (b) photographs of 0.09 cm^2, 1 cm^2, and 4 cm^2 flexible OSCs, (c) J–V characteristics of 0.09 cm^2 and 4 cm^2 flexible OSCs, (d) EQE spectra of 4 cm^2 flexible OSCs, and (e) statistics of device efficiency in different areas.

Table 2 Device performance of the 0.09 and 4 cm^2 flexible solar cells

Area	ETLs	V_{OC} (V)	J_{SC} (mA cm^{-2})	FF	PCE_{max} (%)	PCE_{ave} (%)
0.09 cm^2	ZnO NPs	0.82	23.64	0.70	13.56	13.42 ± 0.05
	Bi-layer 0.1 M	0.82	25.39	0.72	14.97	14.65 ± 0.31
4 cm^2	ZnO NPs	0.80	20.92	0.61	10.21	9.95 ± 0.27
	Bi-layer 0.1 M	0.81	24.85	0.65	13.08	13.03 ± 0.04

device revealed improved carrier extraction at the cathode interface. From the TPV curves, the carrier lifetime in the bilayer ETL-based cells was determined to be 38.4 μs, which was slightly longer than that of the ZnO devices (31.3 μs). This result indicated that the use of the sol–gel ZnO/ZnO NP bilayer ETL has reduced the interface recombination.

On the basis of the above results, the different interface contact properties in the sole ZnO NP and sol–gel ZnO/ZnO NP ETL-based devices could be described in Fig. 5(a). In the case of sole ZnO NP ETLs, the nanoparticles tended to accumulate around the AgNWs, while being less filled in the voids within the networks. The redeposition of a sol–gel ZnO layer could on one hand modify the surface of AgNWs, and on the other hand effectively fill these voids. Both the aspects could enable the formation of a homogeneous ZnO NP layer and improve interface contact and charge extraction ability between the electrode and the active layer. Therefore, enhanced device performance was obtained. Previously, we found a higher sensitivity of large-area doctor-blade OSCs to the interface contact than small-area devices.[48] In large-area OSCs, there are higher possibilities of poor interface charge transport or even current leakage caused by interface nonuniformity and defects.[49] That is a reason for the higher sensitivity of large-area devices to interface contact. Thus, in the case of large-area flexible OSCs, a higher sensitivity of performance to the interface contact would also occur. On the basis of this speculation, we fabricated 0.09 and 4 cm^2 flexible OSCs for comparison, and Fig. 5(b) shows the photographs of these devices. The *J–V* characteristics and EQE spectra of these devices are shown in Fig. 5(c) and (d). Table 2 lists the device performance of these cells. In the case of 0.09 cm^2 small area devices, we found that the cells with the ZnO NP ETL showed an optimized performance and an average performance of 13.56% and 13.42%. With a bilayer ETL, the best performance improved to 14.97%, and the average performance increased to 14.65%. These results showed that the devices with the bilayer ETL have slightly higher efficiencies relative to the device with the sole ZnO NP ETL. As discussed above, the 1 cm^2 device with the bilayer ETL exhibited much higher performance than the sole ZnO NP ETL device. Such results indicated different sensitivities of performance to the ETL for the small-area and 1 cm^2 devices. As the size increased to 4 cm^2, an optimized performance of 10.21% was achieved with the ZnO NP ETL. The devices with the sol–gel ZnO/ZnO NP bilayer ETL showed an optimized efficiency of 13.08%. Fig. 5(e) exhibits the statistics of the device performance of 0.09, 1, and 4 cm^2 flexible solar cells. As shown by this figure, the device efficiency decreased 1.83% and 3.35% (from 13.56% to 11.73% and 10.21%) for the ZnO NP ETL devices with different sizes, and the efficiency decreased 0.68% and 1.89% (from 14.97% to 14.29% and 13.08%) for the sol–gel ZnO/ZnO NP ETL devices. Such a tendency implied the importance of interface contact for large-area flexible OSCs.

Simultaneously, the long-term stability of the devices was tested and is shown in Fig. 6(a). We can find that the efficiency of the ZnO NP ETL-based device was attenuated to about 80% of the original efficiency after 1000 h. The sol–gel ZnO/ZnO NP bilayer ETL cell maintained over 90% of the original device performance. Fig. S5† shows the normalized V_{OC}, J_{SC}, FF, and PCE of the devices during the storage for 1000 hours in a glove box. It showed that the performance degradation of the ZnO NP ETL-based device was mainly originated from the decrease in FF, indicating that the long-term stability was influenced by the interface degradation. A possible reason might be the quicker degradation of the ZnO NPs/active layer interface due to the photocatalytic effect of ZnO.[50–53] The existence of polyvinyl pyrrolidone (PVP) in the Ag networks would induce more interface defects in ZnO NP ETLs, and then accelerated the interface degradation. With a middle sol–gel ZnO layer between the AgNWs and ZnO NPs, these PVP components would not directly contact with the ZnO NP layer. Thus, the stability of the AgNW electrode was improved after the modification of AgNWs with sol–gel ZnO. An improved stability of the flexible AgNW electrode and OSCs was also reported,[54] which was similar to this result. In addition, the PCE degradation of the 1 cm^2 flexible OSCs during continuous bending with a bending radius of 7.5 mm is shown in Fig. 6(b). After 4000 bending cycles, both the two kinds of devices retained 90% of the original efficiency, indicating that the introduction of an additional sol–gel ZnO layer would not impact the mechanical properties of the flexible OSCs.

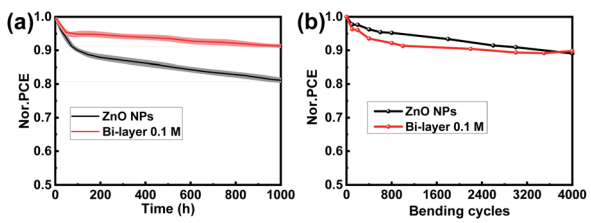

Fig. 6 (a) Long-term stability of the 1 cm^2 flexible solar cells during 1000 h storage in a N_2 filled glove box and (b) PCE degradation of 1 cm^2 flexible OSCs during 4000 bending cycles with a bending radius of 7.5 nm.

Conclusions

In summary, with the aim to achieve high-performance large-area flexible OSCs, we focused on the optimization of the

performance of 1 and 4 cm^2 single cells. With an Ag nanowire as the conducting electrode, we found that the performance of 1 and 4 cm^2 flexible OSCs is more sensitive to the interface contact, while that of small area solar cells is relatively less sensitive. With the traditional ZnO NPs or sol–gel ZnO films as the ETLs, inferior performance was obtained. The introduction of a bilayer ETL based on a thin sol–gel ZnO layer and a ZnO NP layer would improve the interface contact between the AgNW electrode and buffer layer, and greatly improve the optimized performance and the reproducibility of the solar cells. With the bilayer ETLs, a highest performance of 14.29% for the 1 cm^2 and 13.08% for the 4 cm^2 cells was obtained.

Experimental sections

Materials

Silver nanowires dispersed in deionized water and diluted with isopropanol (IPA) were purchased from H&C Advanced Materials Ltd. PBDB-T-2F and Y6 were purchased from Solarmer Materials Inc, Beijing. Zinc acetate was supplied by Aladdin Ltd. 2-Methoxyethanol was purchased from J&K Scientific. Ethanol amine was purchased from Sigma Aldrich.

Preparation of sol–gel ZnO

The ZnO sol–gel precursor was prepared through dissolving zinc acetate in dimethoxy ethanol, with a small amount of ethanolamine as the stabilizer, followed by stirring overnight. In this way, we prepared a series of sol–gel ZnO films on the top of AgNWs with different concentrations of sol–gel ZnO solutions.[40]

OSC fabrication

PET/AgNW electrodes are prepared by gravure printing.[15] The detailed fabrication process is described as follows: the sol–gel ZnO precursor solution with different concentrations was deposited on the top of AgNWs through spin-coating at 2000 rpm for 50 s, and after that the film was annealed at 150 °C for 0.5 h. Afterward, ZnO NPs with a concentration of 15 mg mL^{-1} were spin-coated at 1000 rpm for 60 s, and the film was annealed at 130 °C for 15 min in an air atmosphere and transferred into a N_2-filled glove box to deposit the active layer film. The active layer solution was prepared by dissolving the polymer donor PBDB-T-2F and the small molecular acceptor Y6 in chloroform with a weight ratio of 1 : 1.2 and 0.5 vol% chloronaphthalene (CN). The mixed solution was stirred continuously at 50–60 °C for at least 2 hours. The active layer solution (7 mg mL^{-1} in chloroform) was dynamically spin-coated onto the ZnO NP film at 1000 rpm for 60 s, and after that the active layer was annealed at 100 °C for 10 min. Finally, 15 nm MoO_3 and 200 nm Al were deposited on the active layer film through a shadow mask under a vacuum of 1×10^{-4} Pa.

Characterization

We used a Park XE-120 microscope (NSC18, Mikromasch, Tallinn, Estonia) coated with a Cr/Au conductive tip to record the atomic force microscope (AFM) image of the film. The transmittance spectra were recorded by using a Lambda 750 UV-vis-NIR Spectro-photometer (PerkinElmer). The micrograph was investigated by using a cold field emission Scanning Electron Microscope (SEM, S-4800). The current density–voltage (J–V) measurement was conducted under a Newport solar simulator (100 mW cm^{-2}) and in a nitrogen glove box with a Keithley 2400 source instrument. The external quantum efficiency (EQE) of the cell was measured as a function of wavelength, under simulated one sun operating conditions. We use a 150 W halogen tungsten lamp (Osram 64610), and use a monochromator (Zolix, Omni-λ300) to select the wavelength required for the test. At the same time, we use a silicon solar cell for calibration. For the long-term stability, we stored the devices in a N_2-filled glove box and made the J–V measurement after a period of time. The transient photocurrent (TPC) and transient photovoltage (TPV) of the devices were measured (100 Ω input impedance for transient photocurrent and 5 KΩ for transient photovoltage) by exposing the devices to an excitation pulse from a LED lamp with a wavelength of 520–530 nm and a pulse duration of 100 μs.

Conflicts of interest

There are no conflicts to declare.

Acknowledgements

The work is financially supported by the National Natural Science Foundation of China (51773224), Youth Innovation Promotion Association, CAS (2019317), Ministry of Science and Technology of China (2016 YFA0200700), Vacuum Interconnected Nanotech Workstation Suzhou Institute of Nano-Tech and Nano-Bionics, Chinese Academy of Sciences (CAS).

References

1 Y. Li, G. Xu, C. Cui and Y. Li, *Adv. Energy Mater.*, 2018, **8**, 1701791.
2 J. Hou, O. Inganäs, R. H. Friend and F. Gao, *Nat. Mater.*, 2018, **17**, 119–128.
3 J. Yuan, Y. Q. Zhang, L. Y. Zhou, G. H. Zhang, H.-L. Yip, T. K. Lau, X. H. Lu, C. Zhu, H. J. Peng, P. A. Johnso, M. Leclerc, Y. Cao, J. Ulanski, Y. F. Li and Y. P. Zou, *Joule*, 2019, **3**, 1–12.
4 Y. Cui, H. F. Yao, J. Q. Zhang, K. H. Xia, T. Zhang, L. Hong, Y. M. Wang, Y. Xu, K. Q. Ma, C. B. An, C. He, Z. X. Wei, F. Gao and J. H. Hou, *Adv. Mater.*, 2020, **32**, 1908205.
5 Q. Liu, Y. Jiang, K. Jin, J. Qin, J. Xu, W. Li, J. Xiong, J. Liu, Z. Xiao, K. Sun, S. Yang, X. Zhang and L. Ding, *Sci. Bull.*, 2020, **65**, 272–275.
6 L. Zhan, S. Li, X. Xia, Y. Li, X. Lu, L. Zuo, M. Shi and H. Chen, *Adv. Mater.*, 2021, **33**, 2007231.
7 X. Meng, L. Zhang, Y. Xie, X. Hu, Z. Xing, Z. Huang, C. Liu, L. Tan, W. Zhou, Y. Sun, W. Ma and Y. Chen, *Adv. Mater.*, 2019, **31**, 1903649.
8 K.-H. Choi, J. Kim, Y.-J. Noh, S.-I. Na and H.-K. Kim, *Sol. Energy Mater. Sol. Cells*, 2013, **110**, 147–153.

9 T. Lei, R. X. Peng, L. K. Huang, W. Song, T. T. Yan, L. Q. Zhu and Z. Y. Ge, *Mater. Today Energy*, 2019, **14**, 100334.
10 L. Mao, Q. Chen, Y. W. Li, Y. Li, J. H. Cai, W. M. Su, S. Bai, Y. Z. Jin, C. Q. Ma, Z. Cui and L. W. Chen, *Nano Energy*, 2014, **10**, 259–267.
11 Y. Han, X. Chen, J. Wei, G. Ji, C. Wang, W. Zhao, J. Lai, W. Zha, Z. Li, L. Yan, H. Gu, Q. Luo, Q. Chen, L. Chen, J. Hou, W. Su and C. Q. Ma, *Adv. Sci.*, 2019, **6**, 1901490.
12 J. Kim, D. Ouyang, H. Lu, F. Ye, Y. Guo, N. Zhao and W. C. H. Choy, *Adv. Energy Mater.*, 2020, **10**, 1903919.
13 J.-W. Lim, D.-Y. Cho, K. Jihoon, S.-I. Na and H.-K. Kim, *Sol. Energy Mater. Sol. Cells*, 2012, **107**, 348–354.
14 W. Pan, Y. Han, Z. Wang, Q. Luo, C. Ma and L. Ding, *J. Semicond.*, 2021, **39**, 014002.
15 Z. Wang, Y. Han, L. Yan, C. Gong, J. Kang, H. Zhang, X. Sun, L. Zhang, J. Lin, Q. Luo and C. Q. Ma, *Adv. Funct. Mater.*, 2020, **31**, 2007276.
16 Y. Sun, M. Chang, L. Meng, X. Wan, H. Gao, Y. Zhang, K. Zhao, Z. Sun, C. Li, S. Liu, H. Wang, J. Liang and Y. Chen, *Nat. Electron.*, 2019, **2**, 513–520.
17 X. Chen, G. Xu, G. Zeng, H. Gu, H. Chen, H. Xu, H. Yao, Y. Li, J. Hou and Y. Li, *Adv. Mater.*, 2020, **32**, 1908478.
18 T. Y. Qu, L. J. Zuo, J. D. Chen, X. Shi, T. Zhang, L. Li, K. C. Shen, H. Ren, S. Wang, F. M. Xie, Y. Q. Li, A. K. Y. Jen and J. X. Tang, *Adv. Opt. Mater.*, 2020, **8**, 2000669.
19 Q. Kang, Y. Zu, Q. Liao, Z. Zheng, H. Yao, S. Zhang, C. He, B. Xu and J. Hou, *J. Mater. Chem. A*, 2020, **8**, 5580–5586.
20 B. Fan, Z. Zeng, W. Zhong, L. Ying, D. Zhang, M. Li, F. Peng, N. Li, F. Huang and Y. Cao, *ACS Energy Lett.*, 2019, **4**, 2466–2472.
21 T. Lee, S. Oh, S. Rasool, C. E. Song, D. Kim, S. K. Lee, W. S. Shin and E. Lim, *J. Mater. Chem. A*, 2020, **8**, 10318–10330.
22 G. Wang, M. A. Adil, J. Zhang and Z. Wei, *Adv. Mater.*, 2018, **31**, 1805089.
23 S. Jeong, B. Park, S. Hong, S. Kim, J. Kim, S. Kwon, J.-H. Lee, M. S. Lee, J. C. Park, H. Kang and K. Lee, *ACS Appl. Mater. Interfaces*, 2020, **12**, 41877–41885.
24 Y. W. Han, S. J. Jeon, H. S. Lee, H. Park, K. S. Kim, H. W. Lee and D. K. Moon, *Adv. Energy Mater.*, 2019, **9**, 1902065.
25 Y. Galagan, J.-E. J. M. Rubingh, R. Andriessen, C.-C. Fan, P. W. M. Blom, S. C. Veenstra and J. M. Kroon, *Sol. Energy Mater. Sol. Cells*, 2011, **95**, 1339–1343.
26 G. Wang, J. Zhang, C. Yang, Y. Wang, Y. Xing, M. A. Adil, Y. Yang, L. Tian, M. Su, W. Shang, K. Lu, Z. Shuai and Z. Wei, *Adv. Mater.*, 2020, **32**, 2005153.
27 L. Lucera, F. Machui, P. Kubis, H. D. Schmidt, J. Adams, S. Strohm, T. Ahmad, K. Forberich, H.-J. Egelhaaf and C. J. Brabeca, *Energy Environ. Sci.*, 2016, **9**, 89.
28 Y. Li, L. Mao, F. Tang, Q. Chen, Y. Wang, F. Ye, L. Chen, Y. Li, D. Wu, Z. Cui, J. Cai and L. Chen, *Sol. Energy Mater. Sol. Cells*, 2015, **143**, 354–359.
29 S. Choi, Y. Zhou, W. Haske, J. W. Shim, C. Fuentes-Hernandez and B. Kippelen, *Org. Electron.*, 2015, **17**, 349–354.
30 M. Hambsch, H. Jin, A. J. Clulow, A. Nelson, N. L. Yamada, M. Velusamy, Q. Yang, F. Zhu, P. L. Burn, I. R. Gentle and P. Meredith, *Sol. Energy Mater. Sol. Cells*, 2014, **130**, 182–190.
31 G. Zhao, W. Wang, T.-S. Bae, S.-G. Lee, C. Mun, S. Lee, H. Yu, G.-H. Lee, M. Song and J. Yun, *Nat. Commun.*, 2015, **6**, 9830.
32 T. Yan, W. Song, J. Huang, R. Peng, L. Huang and Z. Ge, *Adv. Mater.*, 2019, **31**, 1902210.
33 S. B. Ambade, R. B. Ambade, S. H. Eom, M.-J. Baek, S. S. Bagde, R. S. Mane and S.-H. Lee, *Nanoscale*, 2016, **8**, 5024–5036.
34 T. Lei, R. Peng, W. Song, L. Hong, J. Huang, N. Fei and Z. Ge, *J. Mater. Chem. A*, 2019, **7**, 3737–3744.
35 W. Zhang, W. Song, J. Huang, L. Huang, T. Yan, J. Ge, R. Peng and Z. Ge, *J. Mater. Chem. A*, 2019, **7**, 22021–22028.
36 K. W. Seo, J. Lee, J. Jo, C. Cho and J. Y. Lee, *Adv. Mater.*, 2019, **31**, 1902447.
37 Y. Tan, L. Chen, F. Wu, B. Huang, Z. Liao, Z. Yu, L. Hu, Y. Zhou and Y. Chen, *Macromolecules*, 2018, **51**, 8197–8204.
38 Y. E. Ha, M. Y. Jo, J. Park, Y.-C. Kang, S. I. Yoo and J. H. Kim, *J. Phys. Chem. C*, 2013, **117**, 2646–2652.
39 D. Zhou, S. Xiong, L. Chen, X. Cheng, H. Xu, Y. Zhou, F. Liu and Y. Chen, *Chem. Commun.*, 2018, **54**, 563–566.
40 J. Kang, K. Han, X. Sun, L. Zhang, R. Huang, I. Ismail, Z. Wang, C. Ding, W. Zha, F. Li, Q. Luo, Y. Li, J. Lin and C.-Q. Ma, *Org. Electron.*, 2020, **82**, 105714.
41 Y. Sun, L. Meng, X. Wan, Z. Guo, X. Ke, Z. Sun, K. Zhao, H. Zhang, C. Li and Y. Chen, *Adv. Funct. Mater.*, 2021, **31**, 2010000.
42 F. S. F. Morgenstern, D. Kabra, S. Massip, T. J. K. Brenner, P. E. Lyons, J. N. Coleman and R. H. Friend, *Appl. Phys. Lett.*, 2011, **99**, 183370.
43 J. Ajuria, I. Ugarte, W. Cambarau, I. Etxebarria, R. Tena-Zaera and R. Pacios, *Sol. Energy Mater. Sol. Cells*, 2012, **102**, 148–152.
44 X. Wen, S. Fang, Y. Xu, N. Zheng, L. Liu, Z. Xie and F. Würthner, *ACS Appl. Mater. Interfaces*, 2019, **11**, 34151–34157.
45 Y. Sun, J. H. Seo, C. J. Takacs, J. Seifter and A. J. Heeger, *Adv. Mater.*, 2011, **23**, 1679–1683.
46 N. K. Elumalai and A. Uddin, *Energy Environ. Sci.*, 2016, **9**, 391–410.
47 X. Chen, B. Zhu, B. Kan, K. Gao, X. Peng and Y. Cao, *J. Mater. Chem. C*, 2019, **7**, 7947–7952.
48 G. Ji, W. Zhao, J. Wei, L. Yan, Y. Han, Q. Luo, S. Yang, J. Hou and C.-Q. Ma, *J. Mater. Chem. A*, 2019, **7**, 212–220.
49 L. Mao, J. Tong, S. Xiong, F. Jiang, F. Qin, W. Meng, B. Luo, Y. Liu, Z. Li, Y. Jiang, C. Fuentes-Hernandez, B. Kippelen and Y. Zhou, *J. Mater. Chem. A*, 2017, **5**, 3186–3192.
50 Y. Y. Jiang, L. L. Sun, F. Y. Jiang, C. Xie, L. Hu, X. Y. Dong, F. Qin, T. F. Liu, L. Hu, X. S. Jiang and Y. H. Zhou, *Mater. Horiz.*, 2019, **6**, 1438–1443.
51 K. Z. Qi, B. Cheng, J. G. Yu and W. K. Ho, *J. Alloys Compd.*, 2017, **727**, 792–820.
52 S. Park and H. J. Son, *J. Mater. Chem. A*, 2019, **7**, 25830–25837.
53 Y. F. Han, H. L. Dong, W. Pan, B. W. Liu, X. Z. Chen, R. Huang, Z. Y. Li, F. S. Li, Q. Luo, J. Q. Zhang, Z. X. Wei and C. Q. Ma, *ACS Appl. Mater. Interfaces*, 2021, **13**, 17869–17881.
54 M. Song, J. H. Park, C. S. Kim, D.-H. Kim, Y.-C. Kang, S.-H. Jin, W.-Y. Jin and J.-W. Kang, *Nano Res.*, 2014, **7**, 1370–1379.